Solution Structure of a DNA·RNA Hybrid Containing an α-Anomeric Thymidine and Polarity Reversals: d(ATGG-3′-3′-αT-5′-5′-GCTC)·r(gagcaccau)[†,‡]

James M. Aramini and Markus W. Germann*

Department of Microbiology and Immunology, Kimmel Cancer Institute, Thomas Jefferson University, Philadelphia, Pennsylvania 19107

Received June 30, 1999; Revised Manuscript Received September 3, 1999

ABSTRACT: We report the thermodynamic and structural properties of an α-containing DNA·RNA nonamer hybrid duplex, d(ATGG-3′-3′-αT-5′-5′-GCTC)·r(gagcaccau). The RNA strand corresponds to the core of the initiation sequence for the transcript of the *erb*B-2 oncogene. The tandem anomeric and polarity changes in the DNA strand result in a slight decrease in thermostability ($\Delta T_m = -2.8$ °C) compared to the unmodified control hybrid. The three-dimensional solution structure determination of the α-containing DNA·RNA hybrid, conducted via restrained molecular dynamics using interproton distance (nuclear Overhauser enhancement) and furanose ring torsion angle (*J*-based) restraints, converged to a final ensemble of structures from unique starting models. In agreement with hyperchromicity and circular dichroism data, the final average structure derived from this ensemble is consistent with an overall A-like motif featuring Watson−Crick base pairing and base stacking across the entire sequence, albeit with localized B-like traits within the DNA strand. Comparative pseudorotation analyses of the *J*-coupling data for this hybrid and its unmodified control reveal a surprising increase in S-puckering for two nucleotides immediately upstream of the 3′−3′ linkage, and the associated narrowing of the minor groove in this portion of the hybrid. Other structural perturbations are localized to and diagnostic of the central α-nucleotide and juxtaposed polarity reversals. The structural information presented here has direct relevance to the design of future antisense oligonucleotides composed of these modifications.

In the last two decades, the development of antisense oligonucleotide (ODN)[1] drugs designed to selectively inhibit the production of an unwanted protein by arresting the translation of its specific RNA message has been intensely pursued (*1*−*3*). To this end, a wide array of modifications to the phosphodiester backbone, sugar, and base components that constitute nucleic acids have been engineered in an effort to enhance several properties thought to be important for this approach (*4*, *5*); these include the stability of the resulting ODN·RNA hybrid, nuclease resistance of the ODN, and the ability of the ODN to elicit RNase H cleavage of the target RNA strand.

The central importance of DNA·RNA hybrids in the antisense strategy, along with their roles in DNA replication, transcription, and reverse transcription, has provided strong impetus for unraveling the interplay between hybrid structure, thermostability, and efficacy as RNase H substrates. Structural studies on both natural and modified sequences have established that DNA·RNA hybrids adopt an overall topology that is intermediate between canonical A- and B-forms, in which the DNA strand is generally thought to be conformationally flexible while the RNA strand is more rigid and A-like (*6*−*11*). In addition, the thermostability of a DNA·RNA hybrid is sensitive to sequence composition (*12*, *13*) and can be manipulated by chemical modifications to the DNA strand according to a set of empirical rules (*5*). However, very few DNA modifications—namely, phosphorothioates (*14*) and -dithioates (*15*), and very recently arabinonucleic acids (*16*) and boranophosphates (*17*)—have been shown to invoke RNase H degradation of the complementary RNA strand.

Featuring a single inversion of stereochemistry at the anomeric carbon (C1′), α-anomeric ODNs exhibit high nuclease resistance (*18*), stable parallel-stranded duplex formation with complementary DNA and RNA strands (*19*−*23*), and the ability to impede mRNA translation and viral growth in vitro (*24*, *25*). Recently, interest in α-ODNs as antisense tools increased with the development of chimeric α/*β*-ODNs containing 3′−3′ and 5′−5′ phosphodiester linkages (*26*, *27*), which, unlike purely α-ODNs (*28*), can elicit the RNase H-mediated destruction of complementary RNA strands (*29*, *30*). Moreover, a set of chimeric 16-mers, featuring stretches of four *β*-anomeric residues separated by 3′-3′-αNt-5′-5′ units and designed specifically against human

[†] This work was supported by a grant from the National Institutes of Health, GM OD55404.

[‡] Brookhaven Protein Data Bank ID 1C2Q; RCSB ID RCSB009406.

* To whom correspondence should be addressed: Tel (215) 503-4581; FAX (215) 923-2117; E-mail mwg@lac.jci.tju.edu.

[1] Abbreviations: CD, circular dichroism; CORMA, complete relaxation matrix analysis; DQF-COSY, double quantum filtered correlated spectroscopy; DSS, 2,2-dimethylsilapentane-5-sulfonate; EDTA, ethylenediaminetetraacetic acid; MARDIGRAS, matrix analysis of relaxation for discerning the geometry of an aqueous structure; MDtar, molecular dynamics using time-averaged restraints; NMR, nuclear magnetic resonance; NOE, nuclear Overhauser enhancement; NOESY, NOE spectroscopy; ODN, oligodeoxyribonucleotide; RANDMARDI, random error MARDIGRAS; rEM, restrained energy minimization; rMD, restrained molecular dynamics; RMSD, root-mean-square deviation; SANDER, simulated annealing with NMR-derived energy restraints; TOCSY, total correlated spectroscopy; WATERGATE, water suppression by gradient-tailored excitation.

10.1021/bi9915418 CCC: $18.00
Published on Web 11/05/1999

FIGURE 1: Sequences of the control and alphaT DNA·RNA nonamer hybrid duplexes and DNA·DNA and RNA·RNA secondary control duplexes. The DNA and RNA nucleotides are labeled with upper- and lowercase letters, respectively; the α-anomeric thymidine is shown in outline type. Arrows indicate the strand polarity in the 5′ → 3′ direction, with the unusual phosphodiester linkages in the DNA strand of the alphaT hybrid denoted by head-to-head (3′−3′) and tail-to-tail (5′−5′) junctions. The sequence numbering scheme used throughout this paper, shown for the alphaT hybrid, is in the 5′ → 3′ direction for both strands (i.e., DNA 5′-A1 to C9-3′; RNA 5′-g10 to u18-3′).

papilloma virus type 16, displayed potent antisense and antitumor activities in cell lines and animal models (*31*).

Although we have extensively investigated the thermodynamic, enzymatic, and structural properties of DNA duplexes containing localized polarity-reversed α-anomeric residues (*30*, *32*−*35*), a combined thermodynamic and structural study of their effects in physiologically relevant DNA·RNA hybrids has not been reported. With this goal in mind, we embarked on a study of a DNA·RNA nonamer hybrid, d(ATGG-3′-3′-αT-5′-5′-GCTC)·r(gagcaccau), in which the DNA strand features a central α-anomeric thymidine flanked by polarity-reversing 3′−3′ and 5′−5′ phosphodiester linkages, along with its unmodified control hybrid and related DNA·DNA and RNA·RNA duplexes (Figure 1). The RNA sequence corresponds to a frequently probed antisense target region in the transcript for the *erb*B-2 oncogene (*36*, *37*), whose overexpression is a marker in a number of cancers, including breast and ovarian (*38*, *39*). The thermodynamic and structural perturbations to the DNA·RNA hybrid due to the tandem changes in anomeric sugar configuration and reversals in strand polarity and their implications for the design of antisense ODNs comprising these modifications will be discussed.

EXPERIMENTAL PROCEDURES

Oligonucleotide Synthesis and Sample Preparation. Solid-phase syntheses of d(ATGGTGCTC), d(ATGG-3′-3′-αT-5′-5′-GCTC), and r(gagcaccau), as well as the complementary strands in the secondary control duplexes, d(GAGCACCAT) and r(auggugcuc), were performed by standard phosphoramidite chemistry and subsequently purified according to the protocols employed in our earlier studies on α-containing DNA duplexes (*32*); the synthesis of the alphaT DNA nonamer proceeded through a 5′-phosphoramidite of αT, and 2′-*O*-*tert*-butyldimethylsilyl protecting groups were used in the RNA synthesis. Prior to use, the purity (>95%) of each desalted (gel filtration) ODN sample was confirmed by denaturing polyacrylamide gel electrophoresis (8 M urea); ^{1}H NMR spectroscopy was also used to verify ODN purity as well as the stoichiometry of duplex samples. Stock solution concentrations for the individual ODNs were determined from the A_{260} of thermally denatured (85 °C) aliquots using the following molar extinction coefficients derived from sums of mononucleoside ϵ_{260} values (*40*) and the sequence composition; ϵ_{260} values (M^{-1} cm^{-1}) were as follows: DNA, 90 800, and RNA, 100 700; complementary DNA and RNA strands, 100 100 and 94 000, respectively. In all experiments, hybrid duplexes were prepared in the following buffer: 50 mM NaCl, 10 mM phosphate, and 0.1 mM EDTA, pH 6.5−7.0. Samples for NMR spectroscopy were exchanged into either 90% H_2O/10% D_2O or 99.996% D_2O (Cambridge Isotopes).

UV Thermal Denaturation and CD Studies. All UV thermal denaturation experiments were performed at $\lambda = 260$ nm on a thermostated multicell Cary 3E spectrophotometer with WinUV software (Varian) using a 0.4 °C/min temperature ramp, a signal averaging time of 2 s, and a data collection interval of 0.1 °C. For each duplex, melting temperatures (T_m) for total strand concentrations (C_T) of 10, 20, 40, and 80 μM were calculated from a minimum of three melting curves at each concentration by use of a six-parameter fitting routine and assuming a two-state, helix ↔ coil transition (*32*, *33*). The salient thermodynamic variables, namely, the enthalpy ($\Delta H°$) and entropy ($\Delta S°$), were subsequently obtained from van't Hoff plots of the concentration dependence of the T_m according to eq 1, which is valid for bimolecular association of non-self-complementary strands (*41*):

$$\frac{1}{T_m} = \frac{R}{\Delta H°} \ln C_T + \frac{\Delta S° - R \ln 4}{\Delta H°} \quad (1)$$

Hyperchomicity profiles were obtained by dividing the absorbances from wavelength scans (330 → 220 nm; 100 nm/min) of the coil and duplex forms acquired at 85 and 5 °C, respectively. Circular dichroism spectra were recorded on a Jasco J-500A spectropolarimeter at room temperature (330 → 210 nm; 20 nm/min) using 2 mm cuvettes and are expressed as $\Delta\epsilon$ (r) per residue (M^{-1} cm^{-1}).

NMR Spectroscopy. NMR experiments described below were performed at 298 K on a Bruker AMX600 NMR spectrometer at resonance frequencies of 600.1 (^{1}H) and 242.9 (^{31}P) MHz, using 5-mm IDTG-600 triple resonance (Nalorac Corp.) and broadband inverse (Bruker) probeheads. The acquisition and processing parameters of the experiments necessary for resonance assignment and structure determination are analogous to those described in our earlier studies (*32*−*34*). Of particular importance are the following conditions: For D_2O experiments, (i) NOESY spectra were obtained at mixing times (τ_m) of 75, 150, and 250 ms with a 10 s relaxation delay, and very weak presaturation of the residual HDO signal, (ii) DQF-COSY spectra were resolution enhanced (0.73 Hz/point) by strip transformation using 45°-shifted sine-bell multiplication in both dimensions, (iii) 2D ^{31}P−^{1}H correlation spectra (*42*) were strip-transformed and processed with 90° shifted sine-bell multiplication in both dimensions; for H_2O experiments: 1−1 jump and return (*43*) and WATERGATE (*44*) NOESY spectra were acquired with a τ_m of 150 ms and 4 s relaxation delay. Assignment of 2D

Table 1: Statistical Data for the Final Restraints Used in the NMR Structure Determination of the alphaT DNA·RNA Hybrid[a]

restraint	number	*k*
Quantitative Distance Restraints (RANDMARDI)		
(1) nonexchangeables (total)	246	25
(i) intraresidue	163	25
(ii) interresidue (sequential)	81	25
(iii) interresidue (cross-strand)	2	25
⟨well⟩[b] (Å)	0.44 ± 0.61	
(2) exchangeables (total)	22	20
⟨well⟩ (Å)	1.47 ± 0.81	
Endocyclic Torsion Angle Restraints ($\nu_0-\nu_4$)		
(1) deoxyribose (pseudorotation analysis)	45	50
⟨well⟩ (deg)	9.2 ± 3.1	
(2) ribose (broad N-type)	45	50
⟨well⟩ (deg)	35.4 ± 15.1	
Watson−Crick Restraints		
distance	23	25
flat angle	23	10
Backbone Torsion Angle Restraints (α, β, γ, ϵ, ζ)		
(1) broad right-handed (rMD only)	72	10
(2) other[c]	1	10
Chirality (Angle) Restraints		
ribose C2′ (rMD only)	9	10
total (rEM)	405	
average restraints per residue (rEM)	22.5	
DNA strand	26.9	
RNA strand	18.1	

[a] Force constants, *k*, for the distance and (torsion) angle restraints are in units of kcal/(mol·Å^2) and kcal/(mol·rad^2), respectively. Average well-width, ⟨well⟩ = $(\sum|r_3 - r_2|)/N$, and standard deviations are shown. [b] If the vicinal intraresidue sugar interproton distances (54) are ignored, ⟨well⟩ increases to 0.49 ± 0.64 Å. [c] A weak, broad (r_2 = 150, r_3 = 210°) γ^t restraint was applied to the α-thymidine during the final stage of the structure determination (see text).

spectra and NOESY cross-peak integration were performed with SPARKY 3.33 (UCSF). Overall rotational correlation times, τ_c, for both control and alphaT hybrid duplexes of 3.3 ± 0.5 ns were obtained from the truncated driven 1D NOE method (*45*). ^{1}H and ^{31}P spectra were referenced to internal DSS and external 85% H_3PO_4 (capillary in D_2O).

Structural Restraints. Empirical restraints were incorporated into the structure calculations in the form of parabolic, flat-well pseudoenergy terms (eq 2), where *k* is the restraint force constant and *r* is the model distance or torsion/bond angle.

$$\begin{aligned} E_{\text{restraint}} &= k(r_2 - r)^2 \qquad r_1 \le r < r_2 \\ E_{\text{restraint}} &= 0 \qquad\qquad\quad r_2 \le r \le r_3 \\ E_{\text{restraint}} &= k(r - r_3)^2 \qquad r_3 < r \le r_4 \end{aligned} \tag{2}$$

A breakdown of the restraints and associated force constants employed in the structure determination of the alphaT DNA·RNA hybrid is given in Table 1. The source and nature of each restraint type are briefly described below (see ref *34*).

(i) Quantitative Distance Restraints. From lists of cross-peak volumes and uncertainties obtained from each of the NOESY data sets in D_2O and H_2O, interproton distance bounds for the nonexchangeable and exchangeable protons were calculated from sets of 30 RANDMARDI runs (MARDIGRAS 3.2; *46*−*48*), performed as a function of rotational correlation time (τ_c = 2.5, 3.5, and 4.5 ns) and structure, assuming isotropic molecular motion, a three-site jump model for methyl group rotation (*49*), and the normalization over all input volumes option. Lower (r_2) and upper (r_3) distance bounds for the nonexchangeable protons represent the averages of the lower and upper bounds from all RANDMARDI runs but were widened ($\pm\sigma$) in cases (≈10%) where the percentage of solutions obtained was below a certain threshold (i.e., 67%). For distances involving exchangeable protons, RANDMARDI calculations were performed with the nonexchangeable distances held fixed and the absence of exchange, resulting in upper bounds only; lower bounds were set to 2.0 Å.

(ii) (Deoxy)ribose Ring Torsion Angle Restraints. Beginning with pseudorotation analyses of vicinal ^{1}H−^{1}H *J*-coupling constants obtained from SPHINX/LINSHA simulations (*50*) of DQF-COSY cross-peaks, endocyclic sugar ring torsion angle restraints ($\nu_0-\nu_4$) for the DNA strand were based on the average value for each individual torsion angle and its uncertainty calculated from the sugar puckering data (pseudorotation phase angles and mole fractions plus uncertainties) as previously described (*34*, *51*). Broad N-type endocyclic torsion angle restraints were applied to each residue in the RNA strand corresponding to a pseudorotation angle range of $-45° \le P \le 45°$ and puckering amplitude, Φ, of 38°, consistent with the qualitative DQF-COSY data for these sugars ($J_{1'2'} \le 2$ Hz; $J_{2'3'} \le 6$ Hz).

(iii) Watson−Crick Restraints. Heavy-atom Watson−Crick distance restraints (*52*) and weak linear (170−190°) hydrogen-bond angle restraints were applied to all nine base pairs in the hybrid duplex. The upper bound of the αT-A base pair distance restraint was increased by 0.3 Å.

(iv) Backbone Torsion Angle Restraints. To maintain helical right-handedness in the simulated annealing rMD runs, the following weak and broad backbone torsion angle restraints were applied (*51*): $\alpha = -90°$ to $-30°$, β = 135−215°, γ = 30−90°, ϵ = 140−300°, and ζ = 150−315°. Backbone torsions within the unusual 3′−3′ and 5′−5′ linkages were left unrestrained, with the exception of a weak, broad γ^t restraint for the α-nucleotide added to the final cycle of the protocol on the basis of the high proportion of this rotamer in the structural ensemble from the first cycle, as well as intraresidue NOE [d_i(3′;5′) and d_i(3′;5″)] and *J*-coupling ($J_{4'5'}$ and $J_{4'5''}$) data for this residue (*34*, *53*).

Structure Determination. All structure generation and calculations were conducted using subroutines (NUCGEN, LEaP, and SANDER) within the AMBER 4.1 package and using the 1994 all-atom nucleic acid parametrization (*54*, *55*). In all cases, charges on the phosphate groups (PO_4) were attenuated to −0.2/nucleotide to mimic the effects of counterions (*51*).

Starting Models. A- and B-form starting models for the control DNA·RNA nonamer hybrid were generated by unrestrained energy minimization (1000 steps of steepest descent plus 4000 steps of conjugate gradient) of initial models based on canonical Arnott A-RNA and B-DNA right-handed templates. Starting A- and B-models of the alphaT DNA·RNA hybrid were produced from these models by substitution of the central thymidine with an αT and the 3′−3′ and 5′−5′ phosphodiester linkages, followed by energy minimization as above.

Table 2: Thermodynamic Data for the Control and alphaT DNA·RNA Nonamer Hybrids and Related DNA·DNA and RNA·RNA Control Duplexes[a]

duplex	$\Delta H°$ (kJ mol^{-1})	$\Delta S°$ (kJ mol^{-1} K^{-1})	T_m (K) ($C_T = 30\ \mu$M)
control	252 (7)	0.706 (0.022)	312.9 (0.1)
alphaT	257 (5)	0.732 (0.017)	310.1 (0.2)
DNA·DNA	268 (9)	0.763 (0.029)	311.1 (0.1)
RNA·RNA	290 (14)	0.791 (0.045)	326.2 (0.2)

[a] Thermodynamic data for all duplexes were obtained under the following buffer conditions: 50 mM NaCl, 10 mM phosphate, and 0.1 mM EDTA, pH 7.0. In each case, the thermodynamic parameters presented were computed from the slope and *y*-intercept and their uncertainties were obtained from a linear regression analysis (OriginGraph 5.0) of the van't Hoff plot ($R > 0.998$; not shown) incorporating the standard deviations in the measured T_m values at each strand concentration. Extrapolation to the approximate NMR concentrations used ($C_T = 2$ mM) yields T_m values of 327.1 (control hybrid) and 323.6 (alphaT hybrid).

Restrained Molecular Dynamics and Energy Minimization. Using the parameters and protocols described in detail in our recent study (*34*), all rMD (30 ps) and rEM calculations were performed in vacuo with a distance-dependent dielectric constant ($\epsilon = r$), a 30 Å cutoff for nonbonded interactions, and SHAKE applied to all bonds during the dynamics runs only. In all rMD runs, a high temperature (600−900 K) simulated annealing protocol with increased force constants (5×) was employed during the initial 12 ps to surmount energy barriers and allow large conformational movement, followed by equilibration at 300 K for the remainder of the run. Final structures for each rMD run were obtained by rEM (200 steps of steepest descent plus 1800 steps of conjugate gradient) of the averaged coordinates from snapshots (every 0.2 ps) of the last 4 ps of the trajectory.

Structure Determination Strategy. Initially, only quantitative experimental distance restraints for the nonexchangeable protons, obtained from RANDMARDI calculations using the starting A- and B-forms of the alphaT hybrid, were employed in four rMD/rEM runs from both starting models using different random seed numbers. An average structure for this first cycle was obtained by averaging the coordinates of the best seven structures of the ensemble (all-atom RMSD = 0.49 Å), followed by rEM. Interproton distance restraints were refined against this first structure using RANDMARDI, and a second cycle of rMD/rEM calculations incorporating all experimental restraints (Table 1) was conducted using the A and B starting models and the final structure from the first cycle. Coordinate averaging of the ensemble of the best nine structures (three from each starting model; RMSD = 0.73 Å) and rEM yielded the final average structure for the alphaT DNA·RNA hybrid. The iterative structure refinement was terminated at this point on the basis of minimal or no changes in the crystallographic and sixth-root *R*-factors (CORMA 5.2; *56*−*58*) and global helical parameters (CURVES 5.1; *59*) between the final structures for the first and second cycles (RMSD = 0.61 Å).

RESULTS

Thermodynamic, Hyperchromicity, and CD Studies. Thermodynamic data for the control and alphaT hybrid duplexes, as well as the DNA and RNA control duplexes; are listed in Table 2. All data were obtained under the same buffer and salt conditions employed in the NMR studies of the hybrids and subsequent structure determination of alphaT. On the basis of $\Delta H°$ and T_m, the thermostability of this family of duplexes decreases in the order RNA·RNA ≫ control DNA·RNA ≥ DNA·DNA ≥ alphaT DNA·RNA. The combination of the unnatural α-anomeric nucleotide and flanking 3′−3′ and 5′−5′ phosphodiester linkages results in a relatively minor decrease to the thermal stability of the alphaT hybrid compared to the control hybrid. The observed drop in melting temperature for the alphaT hybrid ($\Delta T_m = -2.8$ °C) is quite similar to the effect reported for the same modifications inserted into each strand of a self-complementary DNA decamer duplex ($\Delta T_m = -2.5$ °C/strand), albeit in the presence of increased salt ([NaCl] = 400 mM) to prevent interference in the melting due to unwanted hairpin formation (*32*).

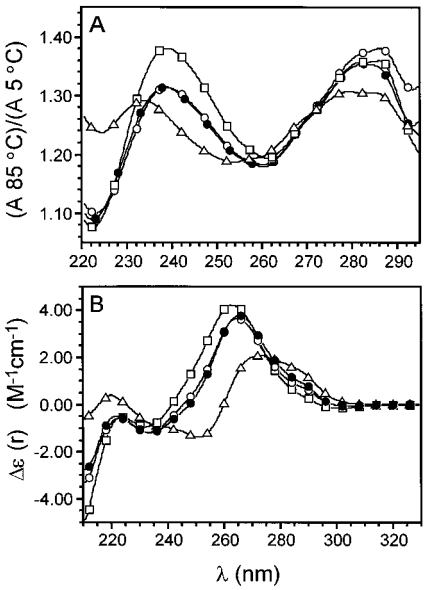

FIGURE 2: (A) Hyperchromicity and (B) circular dichroism spectra for the control DNA·RNA hybrid (○), alphaT DNA·RNA hybrid (●), RNA·RNA duplex (□), and DNA·DNA duplex (△). Symbols indicate every 30th point. Total strand concentrations (C_T) of 10 and 80 μM were used in the UV and CD experiments, respectively.

Hyperchromicity and CD analysis of these duplexes affords a direct comparison of the relative changes in overall stacking and global conformation within the context of an identical sequence (Figure 2). For the DNA·DNA and RNA·RNA duplexes we observe typical B- and A-type CD spectra, respectively, as well as significant differences in the hyperchromicity profiles. The CD and UV spectra for the DNA·RNA hybrids are essentially superimposable and are consistent with, but not identical to, an overall A-like motif quite distinct from the classic B-DNA traits. In general, the thermostability and optical spectroscopic properties of these duplexes are characteristic of DNA·RNA hybrids with mixed sequence (*12*).

NMR Spectroscopy. Near-complete ^{1}H and ^{31}P chemical shift assignments for the control and alphaT DNA·RNA hybrids were attained from standard 2D experiments (NOESY, DQF-COSY, TOCSY, and ^{31}P−^{1}H correlation) and established criteria (*60*). Chemical shift perturbations between the control and alphaT hybrids are essentially localized to the base pair involving the α-anomeric nucleotide and adjacent residues. These changes include significant shifts

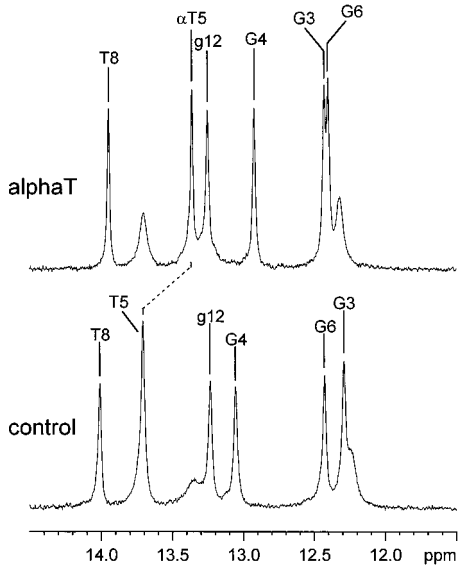

FIGURE 3: Imino region of 1−1 jump and return ^{1}H NMR spectra of the control (1.0 mM) and alphaT (0.89 mM) DNA·RNA hydrids at 283 K. The chemical shift change for the imino proton of the central thymidine is shown with a dashed line. Exchange-broadened imino protons at the ends of the duplexes were not assigned. In both cases, virtually identical resonance patterns were observed down to micromolar concentrations, consistent with duplex formation under optical conditions (data not shown; *32*, *33*).

to the imino proton signal for αT5 (Figure 3), several sugar ring protons in the α-nucleotide, particularly H2′, H2″, and H4′, and the ^{31}P signals of αT5 (3′−3′ linkage) and G6 (5′−5′ linkage); all trends are analogous to those documented for DNA duplexes containing such modifications (*32*, *33*). The resonances corresponding to the RNA strand exhibit very little if any chemical shift differences between the two hybrids. Continuous H1′−H6/H8 NOESY walks [d_i(6,8;1′) → d_s(1′;6,8)],[2] diagnostic of A- and B-form helices, are observed in both strands. However, the H2′/H2″−H6/H8 NOESY pathway [d_i(6,8;2′) → d_s(2″;6,8)] in the DNA strand is interrupted between αT5 and G6, due to the reversed orientation of the sugar moiety in the α-nucleotide (vide infra); this also results in unusual NOE contacts between sugar protons in αT5 and the preceding nucleotide, G4 [i.e., d_s(1′;2′,2″)] (*32*, *33*). The α-nucleotide also features an expected strong intraresidue H4′ to base interaction [d_i(6,8;4′)] (*23*, *32*, *33*). Moreover, several classic A-like NOE cross-peaks were evident, particularly in the RNA strand, including strong H2′/H3′ sugar to base interactions [d_s(2′;6,8), d_i(6,8;3′), d_s(3′;6,8)], as well as most sequential and cross-strand NOE contacts involving adenosine H2 protons [d_s(2;1′), d_{ps}(A2+,2;X1−,1′)].

Pseudorotation Analysis. It is well established that through-bond *J*-coupling constants between protons on adjacent carbon atoms provide an excellent probe of the conformational dynamics of furanose rings in nucleic acids (*61*). On the basis of four key vicinal coupling constants—$J_{1'2'}$, $J_{1'2''}$, $J_{2'3'}$, and $J_{2''3'}$—elucidated by DQF-COSY cross-peak simulations using standard methods (*34*, *62*), puckering information for the deoxyribose moiety of each nucleotide in the DNA strands of the alphaT and control DNA·RNA hybrids (Table 3) was deduced by the pseudorotation analysis method pioneered by Altona and co-workers (*61*, *63*). In this approach, where one assumes that the observed *J*-couplings reflect a rapid two-state equilibrium between N- and S-type sugar puckers, solutions for the puckering amplitude (Φ), pseudorotation phase angle (*P*), and mole fractions of both conformers (f_N and f_S) are obtained from contour plots of the salient *J*-coupling constants as a function of the *P* and *f* for one (major) conformer at a range of Φ values and at a fixed value of *P* for the other (minor) conformer; Φ and *P* represent the maximum displacement of atoms in the ring from planarity and which ones are displaced, respectively. Analogous to our results for the α-containing DNA decamer duplex (*34*), we find that the α-anomeric thymidine exhibits a strong tendency for adopting a distinct S-pucker in the C3′-*exo* to C4′-*endo* range with a slightly reduced amplitude. An approximately equal proportion of N- and S-conformers is predicted for the β-anomeric nucleotides at the ends of the DNA strand (A1, T8, and C9). However, the puckering behavior of the residues on either side of the modified central nucleotide are distinctly different. Nucleotides upstream of αT5 and the 3′−3′ linkage (T2, G3, and G4) display increasing S-pucker character (C1′-*exo* to C2′-*endo*), whereas G6 and especially C7 show a marked preference for the N-conformer (C2′-*exo* to C3′-*endo*). The H3′−H4′ cross-peak data for this hybrid are in qualitative agreement with these results, in accordance with the sensitivity of $J_{3'4'}$ to sugar ring conformation (data shown).[3] Analogous pseudorotation analyses of the *J*-coupling data for the deoxyribose sugars in the control hybrid reveals whether these trends are solely due to sequence effects (Figure 4). Clearly, both G3 and G4 experience a very dramatic increase in S-character in going from the control to the modified hybrid, whereas the shift toward the N-pucker conformation for G6 and C7 is less pronounced. In all cases, the coupling data could not be explained by a single intermediate conformation (i.e., O4′-*endo*, $P = 90°$). Moreover, RANDMARDI-derived intraresidue H1′−H4′ distances across the DNA strand are much larger (3.1 ± 0.2 Å excluding αT5) than the value predicted for the O4′-*endo* pucker (≈2.2 Å; *60*), consistent with no significant population of this conformer. With respect to the RNA strand, the miniscule or completely absent H1′−H2′ DQF-COSY cross-peaks across the sequence are diagnostic of a high proportion of N-puckering; the severe resonance overlap among the ribose sugar protons precludes a comprehensive pseudorotation analysis.

NMR Structure of the alphaT DNA·RNA Hybrid. Driven by the experimental interproton distance and furanose ring torsion angle restraints, the structure determination of the alphaT DNA·RNA hybrid resulted in convergence from different starting points into an ensemble of structures (RMSD = 0.73 ± 0.22 Å),[4] from which a final average structure was calculated (Figure 5A). The final hybrid structure features low distance and torsion angle restraint

[2] We use the nomenclature of Wüthrich (*60*) to represent interproton (NOE) distances. For two nuclei A and B, d_i(A;B) denotes an intraresidue distance; d_s(A;B) represents a sequential (same strand) contact between nonlabile protons, where A and B are in the 5′ and 3′ nucleotides; d_{ps}(A2+,2;X1−,1′), signifies the cross-strand distance between the H2 of adenosine at position 2 in one strand (+) and the H1′ of the nucleotide (X) in the opposite strand (−) across from position 1.

[3] The deoxyribose H3′−H4′ DQF-COSY cross-peaks increase in magnitude with increasing f_N; this cross-peak is vanishingly small in the case of the α-nucleotide.

Table 3: Coupling Constant and Pseudorotation Data for the alphaT and Control DNA·RNA Hybrids[a]

residue	$J_{1'2'}$ (Hz)	$J_{1'2''}$ (Hz)	$J_{2'3'}$ (Hz)	$J_{2''3'}$ (Hz)	$J_{2'2''}$ (±0.5 Hz)	Φ_m (deg) (± 1°)	P (deg)	f_S
				alphaT Hybrid				
A1	6.8 ± 0.5	6.1 ± 0.4	6.0 ± 0.4	4.5 ± 0.7	−14.0	37	135−170	0.54−0.66
T2	9.2 ± 0.7	5.8 ± 0.7	6.2 ± 0.5	< 2.5	−14.0	36	130−155	0.79−0.93
G3	9.4 ± 0.5	5.7 ± 0.4	5.7 ± 0.4	< 2.5	−14.0	36	140−170	0.81−0.95
G4	9.8 ± 0.5	5.7 ± 0.4	5.7 ± 0.4	< 2.5	−14.5	36	140−170	0.85−0.98
αT5	8.3 ± 0.5	3.0 ± 0.7	6.0 ± 0.5	< 2.5	−17.0	33	200−225	0.80−1.00
G6	3.5 ± 0.7	7.1 ± 0.5	6.2 ± 0.5	6.7 ± 0.7	−14.0	36	−15−30	0.23−0.35
C7	3.0 ± 0.7	7.2 ± 0.5	6.6 ± 0.5	8.5 ± 0.7	−14.0	37	−15−30	0.10−0.24
T8	6.4 ± 0.7	6.4 ± 0.7	6.4 ± 0.5	5.5 ± 0.7	−14.0	37	120−165	0.46−0.56
C9	6.5 ± 0.5	6.8 ± 0.4	6.7 ± 0.4	5.5 ± 0.7	−14.5	37	115−145	0.49−0.57
				Control Hybrid				
A1	6.6 ± 0.5	6.4 ± 0.4	6.1 ± 0.4	5.3 ± 0.7	−14.0	37	135−175	0.50−0.59
T2	9.2 ± 0.5	5.8 ± 0.7	6.2 ± 0.5	< 2.5	−14.0	36	130−160	0.79−0.91
G3	nd	nd	nd	nd	nd	nd	nd	0.46 ± 0.15
G4	5.5 ± 0.5	6.5 ± 0.7	6.3 ± 0.5	6.0 ± 1.0	−14.5	36	130−185	0.40−0.53
T5	6.9 ± 0.5	6.4 ± 0.4	6.2 ± 0.4	4.5 ± 1.0	−14.5	36	130−170	0.54−0.67
G6	nd	nd	nd	nd	nd	nd	nd	0.51 ± 0.15
C7	4.9 ± 0.7	7.2 ± 0.5	6.5 ± 0.5	6.9 ± 0.7	−14.5	37	−10−45	0.23−0.41
T8	6.5 ± 0.5	6.5 ± 0.7	6.2 ± 0.5	nd	−14.5	36	130−190	0.50−0.65
C9	6.5 ± 0.5	6.8 ± 0.4	6.7 ± 0.4	5.5 ± 0.7	−14.5	37	115−145	0.49−0.57

[a] Pseudorotation analyses were performed graphically using contour plots of the individual coupling constants as a function of f_S (f_N) and P_S (P_N) at various Φ values assuming the following: β-anomeric sugars A1−G4, T8, C9, $P_N = 18°$ and $\Phi_N = \Phi_S$; high N β-anomeric sugars G6 and C7, $P_S = 153°$ and $\Phi_N = \Phi_S$; αT5, $P_N = 0°$ and $\Phi_N = 37°$. The range of pseudorotation angles listed correspond to the solutions for the major conformer (P_N for G6 and C7; P_S for the others). For both G3 and G6 in the control hybrid, the ^{1}H NMR signals for H2′ and H2″ are completely degenerate, precluding a complete pseudorotation analysis; f_S values for these sugars were estimated from the sum of $J_{1'2'}$ and $J_{1'2''}$ ($\Sigma 1'$) derived from resolution-enhanced DQF-COSY cross-peaks, assuming a two-state equilibrium in which $P_N = 18°$, $P_S = 153°$, and $\Phi_N = \Phi_S = 37°$ (i.e., $f_S = [\Sigma 1' - 9.3]/6.8$). nd, not determined. The expected coupling constants (in hertz) for the O4′-*endo* pucker ($P = 90°$, $\Phi_m = 36°$) are as follows: $J_{1'2'} = 8.5$, $J_{1'2''} = 7.1$, $J_{2'3'} = 8.4$, $J_{2''3'} = 3.0$, and $J_{3'4'} = 6.7$ (*63*).

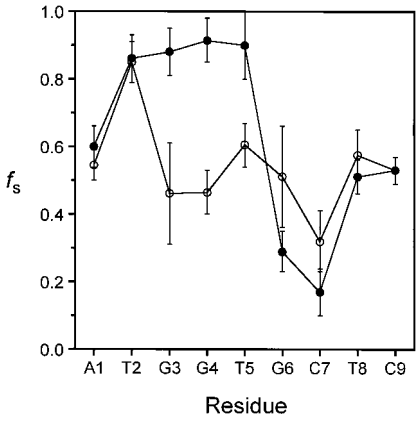

FIGURE 4: Plots of the mole fraction of S-conformer determined by pseudorotation analysis of *J*-coupling data per deoxyribose residue for the control (○) and alphaT (●) DNA·RNA hybrids.

energies, E_{NOE} and E_{tors}, and violations, Δd_{av} and $\Delta \nu_{av}$, compared to the starting A- and B-models, particularly the latter (Table 4). Moreover, only two distance violations over 0.5 Å were observed for the final structure, both in the terminal A1 residue, and no torsion angle violations above 5° were seen. In addition, the final alphaT hybrid structure exhibits low CORMA *R*-factors ($R^x = 4.1-5.3\%$) for the nonexchangeable interproton cross-peak data across the series of NOESY spectra in D_2O (Table 5).

[4] Note that the apparent fraying at the ends of the duplex in the ensemble is actually due to subtle differences in global conformation emanating from local perturbations at the center of the helix due to the modifications, as judged by superimposing the structures in short segments (1−3 base pairs). While the structures reported here are representative of the global fold generated in the vast majority of rMD test runs with a variety of parameters, structures occasionally varied in RMSD up to ≈1.3 Å, yet the local agreement was excellent.

Consistent with the hyperchromicity and CD results discussed earlier, the global secondary structure of the alphaT hybrid is closer to that of an A-form, as judged by pairwise RMSDs with the minimized starting models employed in the structure determination (Table 4). Furthermore, the α-anomeric nucleotide fits snugly into the helix, with the unusual linkages facilitating normal Watson−Crick hydrogen bonding and base stacking, and a concomitant reversal in the orientation of the sugar moiety (Figure 5B).

Analysis of the Final alphaT DNA·RNA Structure. In the following subsections we discuss the pseudorotation phase angles, glycosidic and backbone torsion angles, and selected global helical parameters from the final alphaT DNA·RNA hybrid structure collected in Figure 6.

(i) Deoxyribose Ring Conformation. Analysis of the final alphaT hybrid structure obtained with all experimental restraints and the structure after the first cycle of the protocol, in which only the NOE restraints were enforced, revealed only minimal changes to the sugar ring conformation across the entire molecule. This indicates that the distance and torsion angle restraints are in good agreement, despite the quite different behavior of interproton NOEs and *J*-coupling constants in the presence of conformational exchange. In general, the ribose sugars in the RNA strand reside in the C3′-*endo* (N-pucker) window of the pseudorotation cycle, consistent with a canonical A-type structure. However, in the DNA strand of the final average structure, the terminal nucleotides (i.e., A1, T8, and C9) exhibit pseudorotation phase angles intermediate between N- and S-puckers, while T2−G4 and G6/C7 increasingly gravitate toward values diagnostic of canonical B- and A-motifs, respectively. This behavior exactly follows the pseudorotation anlysis results presented above and is also consistent with per-residue R^x factors against the starting A- and B-models, as well as

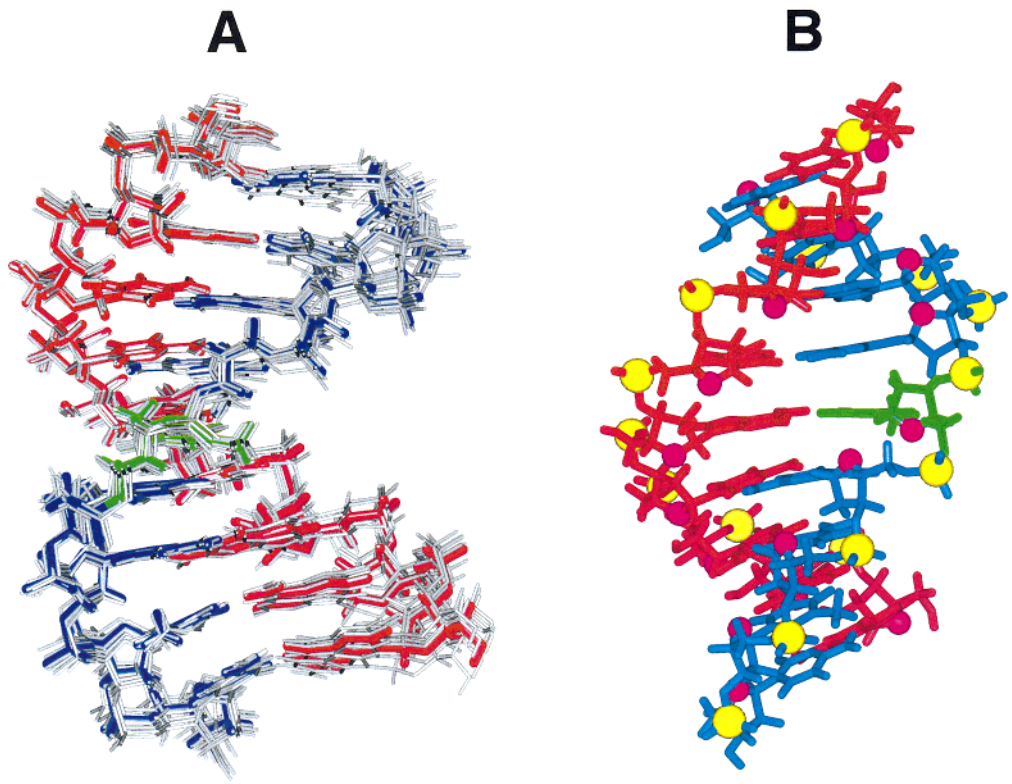

FIGURE 5: (A) Overlay of the ensemble of the best nine rMD/rEM structures (gray) and the final structure of the alphaT DNA·RNA hybrid in which αT5 is shown in green, the remainder of the DNA strand is in blue, and the RNA strand is in red (A1-u18 base pair at top). (B) View into the minor groove of the final alphaT DNA·RNA structure depicted in the same color scheme used above; P (yellow) and O4′ (magenta) atoms in both strands are shown in CPK format (0.5×).

Table 4: Energies, Restraint Violations, and Pairwise All-Atom RMSDs for the Starting Models and Final NMR Structure of the alphaT DNA·RNA Hybrid[a]

structure	E_{AMBER} (kcal/mol)	E_{NOE} (kcal/mol)	E_{tors} (kcal/mol)	Δd_{av} (Å)	$\Delta \nu_{av}$ (deg)	RMSD vs B (Å)	RMSD vs final (Å)
A	−868.2	1848.7	104.7	0.27	10.3	4.5	1.5
B	−870.4	3609.7	265.3	0.39	21.8		3.6
final	−794.8	101.6	1.28	0.067	0.44		

[a] Values for the energies and restraint violations were obtained from one-step rEM computations using the final 405 restraints (no backbone restraints were included); Δd_{av} and $\Delta \nu_{av}$ correspond to the average distance and torsion angle deviations from the upper (if $r > r_3$) or lower (if $r < r_2$) bounds. The initial unminimized canonical A- and B-models of the control hybrid differ by an RMSD of 5.0 Å.

Table 5: Crystallographic (R) and Sixth-Root (R^x) R-Factors for the Starting Models and Final NMR Structure of the alphaT DNA·RNA Nonamer Hybrid[a]

τ_m (ms)	structure	R_{intra}	R_{inter}	R_{total}	R^x_{intra}	R^x_{inter}	R^x_{total}
75	A	0.361	0.626	**0.418**	0.090	0.111	**0.095**
	B	0.492	0.849	**0.569**	0.106	0.227	**0.137**
	final	0.267	0.254	**0.265**	0.053	0.053	**0.053**
150	A	0.358	0.561	**0.405**	0.090	0.098	**0.092**
	B	0.438	0.800	**0.521**	0.087	0.181	**0.115**
	final	0.230	0.260	**0.237**	0.044	0.049	**0.046**
250	A	0.344	0.524	**0.382**	0.081	0.084	**0.082**
	B	0.403	0.695	**0.464**	0.078	0.153	**0.100**
	final	0.214	0.255	**0.223**	0.040	0.043	**0.041**

[a] Total crystallographic ($R = \sum|a_o(i) - a_c(i)|/\sum|a_o(i)|$) and sixth-root ($R^x = \sum|a_o(i)^{1/6} - a_c(i)^{1/6}|/\sum|a_o(i)^{1/6}|$) R-factors (*58*) are listed in separate columns in boldface type. For each NOE data set, R-factors were calculated assuming a τ_c of 3.5 ns, and the total number of unique interproton cross-peak volumes employed in the CORMA calculations are as follows: τ_m = 75 ms, 167; τ_m = 150 ms, 220; τ_m = 250 ms, 256.

RANDMARDI distances for intraresidue and sequential base (H6/H8) to sugar protons (H2′, H2″, H3′) that are highly sensitive to the nature of the sugar pucker and duplex secondary structure (*60*; data not shown). Hence, as the conformational dynamics increase, the conformation of the sugar in the model is pushed into an increasingly intermediate pucker because the restraints cannot be reconciled by a single conformer. This also validates the use of pseudorotation analysis of *J*-coupling data as a structure-independent approach to describing the conformation and dynamics of the deoxyribose moieties. In agreement with the experimental (*J*) pseudorotation results, the pseudorotation phase angle of the α-anomeric is larger ($P = 222°$) than values typical of β-anomers in normal B-DNA.

(ii) Glycosidic (χ) and Backbone (α, β, γ, δ, ϵ, and ζ) Torsion Angles. In the RNA strand, the conformation about the glycosidic bond, which reflects the relative orientation of the base and sugar moieties, and the six backbone torsion angles are highly consistent with values for the canonical A-RNA duplex. In broad terms, values for these structural parameters range from one extreme to the other in the DNA strand, with the trends in the sugar puckering behavior across the sequence discussed above mirrored in the behavior of χ and δ. Glaring exceptions to this are apparent for the central αT5, namely, a dramatic change in χ and shifts in α from g^- to g^+, γ from g^+ to *t*, and ϵ from *t* to g^-. While the radical shift in χ can be purely attributed to the change in stereochemistry at C1′ (*20*, *34*), the altered backbone torsions are characteristic of the unnatural 3′−3′ and 5′−5′ phosphodiester linkages (*34*). Moreover, homo- ($J_{4'5''}$) and het-

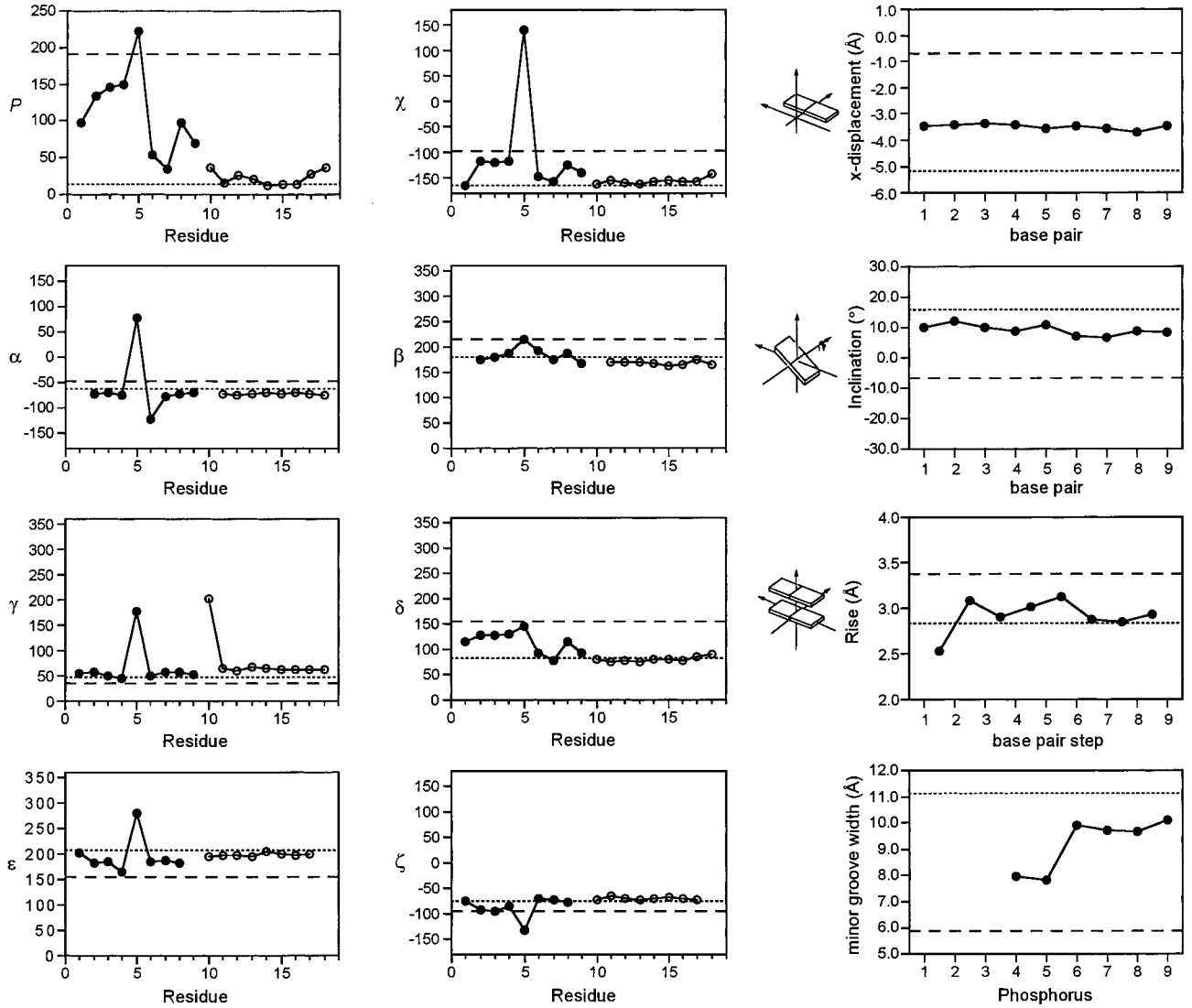

FIGURE 6: Plots of *P*, *χ*, backbone torsion angles (α, *β*, *γ*, *δ*, *ϵ*, and *ζ*), selected global helicoid parameters (*x* displacement, inclination, and rise), and minor groove width for the final structure of the alphaT DNA·RNA hybrid duplex. In graphs of parameters plotted per residue, data for the DNA and RNA strands are depicted as closed and open circles, respectively. For each parameter, the average values for canonical A-RNA and B-DNA duplexes of the same sequence are shown as dotted and dashed lines, respectively. The polarity reversals shuffle the order of the atoms along the backbone necessitating the following definitions for the *ζ* and α torsion angles which characterize the conformation of the 3′−3′ and 5′−5′ linkages (*34*): $\zeta_{(\alpha-1)}$ = C3′(α − 1)−O3′(α − 1)−P(α)−O3′(α), $\zeta_{(\alpha)}$ = O3′(α − 1)−P(α)−O3′(α)−C3′(α), $\alpha_{(\alpha)}$ = C5′(α)−O5′(α)−P(α + 1)−O5′(α + 1), and $\alpha_{(\alpha+1)}$ = O5′(α)−P(α + 1)−O5′(α + 1)−C5′(α + 1), where (α − 1) and (α + 1) represent the nucleotides preceding and following the α-nucleotide. The minor groove width corresponds to the minimum interstrand P−P distance minus 5.8 Å (*65*).

eronuclear ($J_{H3'P}$) three-bond couplings, obtained from simulations of the relevant $^{31}P-^{1}H$ correlation cross-peaks (*34*, *53*, *64*), corroborate the results for *γ* and *ϵ*; specifically, a large $J_{H3'P}$ (≈ 8 Hz) is consistent with the ϵ^- rotamer, and an intermediate value of $J_{4'5''}$ (≈ 6 Hz) is indicative of an ≈50:50 population of γ^+ and γ^t (data not shown). Although the α (5′−5′) and *ζ* (3′−3′) torsion angles of the α-nucleotide are silent by NMR, all of the localized backbone perturbations in this hybrid are highly analogous to those reported for [d(GCGAAT-3′-3′-αT-5′-5′-CGC)]$_2$ (*34*). Moreover, time-averaged rMD trajectories on the latter further indicate that the 5′−5′ linkages are highly fluxional, while the 3′−3′ linkages are relatively static (J. M. Aramini, A. Mujeeb, and M. W. Germann, unpublished results).

(iii) Helicoid Parameters and Minor-Groove Width. Selected global helical parameters that are among the most highly discriminatory of A- and B-motifs, namely, the *x*-displacement from the helical axis (dx), inclination (*η*), and rise (Dz), are consistent with the picture that the alphaT hybrid adopts global conformation toward that of, but not identical to, canonical A-RNA; the latter features significant dx into the minor groove, large positive *η*, and low Dz. The minor-groove width, determined via interstrand phosphorus distances (*65*), is intermediate between those of canonical A-RNA and B-DNA. The dichotomous B- and A-like traits of the residues prior to and following the modifications in the DNA strand are yet again manifest in terms of a narrower minor groove in the 5′- portion of the molecule (with respect to the DNA strand) and a wider minor groove in the 3′-region.

DISCUSSION

Using conventional restrained molecular dynamics driven by interproton distance and furanose ring torsion angle

restraints deduced from the complete relaxation matrix approach and pseudorotation analysis, we have elucidated the average solution structure of a DNA·RNA nonamer duplex containing an α-anomeric thymidine and juxtaposed 3′−3′ and 5′−5′ phosphodiester linkages at the center of the DNA strand. In agreement with CD and UV hyperchromicity data, the hybrid adopts an overall right-handed A-like structure, with the polarity-reversed α-nucleotide correctly positioned for preservation of Watson−Crick base pairing and stacking throughout the duplex. A comparison of the pseudorotation properties of the deoxyribose moieties in the alphaT and control hybrids, however, reveals a dramatic increase in the percentage of S-character for two nucleotides immediately preceding the 3′−3′ linkage and a more subtle shift toward the N-pucker for the two residues following the 5′−5′ linkage. This is complementary to our earlier structural studies on self-complementary DNA duplexes, systems featuring high f_s deoxyribose sugars, in which the profound effect of the 5′−5′ linkage could be easily observed (*32*−*34*). Other structural perturbations in the alphaT hybrid localized to the α-nucleotide and unusual linkages include the reversal in the orientation of the sugar ring for αT5 with respect to the other nucleotides in the DNA strand as well as altered torsion angles in the malleable phosphodiester backbone.

Placing the results presented in this paper within the context of the current picture of the thermodynamics and structural properties of DNA·RNA hybrids and the influence of the latter on RNase H action, we can draw some important conclusions relevant to the design of antisense ODNs containing α-anomeric and 3′−3′ and 5′−5′ phosphodiester linkages. First, it has been widely demonstrated that one of the factors correlated with DNA·RNA stability is the puckering state of the DNA strand. In general, sugar and/or backbone modifications that promote an increase in the N-character of the sugar components within the DNA strand translate into increased thermostability (*5*). In this light, we predict that, while the 5′−5′ linkage appears to be a favorable modification, the dramatic and undesireable shift in sugar puckering upstream of the 3′−3′ linkage may at least partially account for the lower thermodynamic stability of the modified hybrid compared to the control and that modifications that alleviate or counteract the effects of this linkage would result in increased hybrid stability. Second, the fluxional nature of a number of deoxyribose residues predicted by the NOE (alphaT) and *J*-coupling (control and alphaT) data cannot be adequately described by a single structure. This is in accordance with the prevailing dogma, which favors the description of the deoxyribose puckering behavior in terms of an equilibrium between N (C3′-*endo*) and S (C2′-*endo*) conformers rather than residing in an intermediate (i.e., O4′-*endo*) window of conformation (*7*, *10*, *11*, *13*, *66*, *67*), although this has been a point of contention (*6*, *9*). In this context, molecular dynamics with time-averaged restraints (MDtar) and ensemble approaches have been shown to be possible routes for satisfying the NMR data due to dynamic substituents in such molecules (*7*, *10*, *11*); we are currently using the final alphaT hybrid structure as the starting point for further structural calculations using MDtar. Finally, the modifications in the alphaT hybrid result in local alterations to the minor groove width of the duplex coincident with the relative B- to A-like traits observed across the DNA strand. However, the actual importance of DNA·RNA minor-groove width on the action of RNase H (*6*) is unclear in light of mounting evidence suggesting an induced-fit model of substrate−enzyme interaction (*68*−*70*). Interestingly, sequences with alternating β-stretches and single α-nucleotides separated by polarity reversals can elicit RNase H cleavage of complementary RNA strands in vitro (*30*, *31*). In the structure of the alphaT hybrid presented here, the reversal of the orientation of the α sugar results in a displacement of the O4′ away from its normal position in the wall of the minor groove (Figure 5B). Since RNase H is a minor-groove-binding protein and modifications to the DNA strand that protrude into this groove are detrimental to catalysis (*6*, *71*, *72*), we think that the reversal of sugar ring orientation may be more important for the documented inability of fully α-anomeric ODNs to induce RNase H activity, rather than the global structure of α-ODN·β-RNA hybrids (*22*). A recent report of the RNase H substrate properties of arabino-ODN·RNA hybrids (*16*), in which the subsituent at C2′ juts into the major groove, adds further credence to this notion.

We are currently applying the thermodynamic and structural insights gained from the modified DNA·RNA hybrid presented here, as well as related ODNs that have revealed the adverse effects of the combination of αC and the polarity reversals in both DNA and DNA·RNA duplexes (*33*; Aramini and Germann, unpublished results), into the design of α-containing ODNs against the *erb*B-2 target.

ACKNOWLEDGMENT

We thank Dr. Richard T. Pon and the Nucleic Acid Facility at the University of Calgary for synthesizing the ODNs used in this study, Dr. Eric Wickstrom (Thomas Jefferson University) for use of the UV spectrophotometer, and Dr. Anwer Mujeeb (University of California, San Francisco) for helpful discussions and insights regarding the structure determination and analysis.

SUPPORTING INFORMATION AVAILABLE

Tables of ^{1}H and ^{31}P NMR resonance assignments for the alphaT and control hybrids, plots of ^{1}H and ^{31}P chemical shift differences between the alphaT and control hybrids, complete table of energies for the final alphaT hybrid structure, plots of all global helical parameters of the final alphaT hybrid structure obtained by CURVES 5.1, and plots of CORMA R^x factors per residue vs the starting A- and B-models of the alphaT hybrid. This material is available free of charge via the Internet at http://pubs.acs.org.

REFERENCES

1. Lönnberg, H., and Vuorio, E. (1996) *Ann. Med. 28*, 511−522.
2. Agrawal, S., and Iyer, R. P. (1997) *Pharmacol. Ther. 76*, 151−160.
3. Crooke, S. T. (1998) in *Handbook of Experimental Pharmacology* (Crooke, S. T., Ed.) Vol. 131, pp 1−50, Springer-Verlag, Berlin.
4. De Mesmaeker, A., Häner, R., Martin, P., and Moser, H. E. (1995) *Acc. Chem. Res. 28*, 366−374.
5. Freier, S. M., and Altmann, K.-H. (1997) *Nucleic Acids Res. 25*, 4429−4443.
6. Fedoroff, O. Y., Salazar, M., and Reid, B. R. (1993) *J. Mol. Biol. 233*, 509−523.

7. González, C., Stec, W., Reynolds, M. A., and James, T. L. (1995) *Biochemistry 34*, 4969−4982.
8. Cross, C. W., Rice, J. S., and Gao, X. (1997) *Biochemistry 36*, 4096−4107.
9. Fedoroff, O. Y., Ge, Y., and Reid, B. R. (1997) *J. Mol. Biol. 269*, 225−239.
10. Gyi, J. I., Lane, A. N., Conn, G. L., and Brown, T. (1998) *Biochemistry 37*, 73−80.
11. Bachelin, M., Hessler, G., Kurz, G., Hacia, J. G., Dervan, P. B., and Kessler, H. (1998) *Nat. Struct. Biol. 5*, 271−276.
12. Ratmeyer, L., Vinayak, R., Zhong, Y. Y., Zon, G., and Wilson, W. D. (1994) *Biochemistry 33*, 5298−5304.
13. Gyi, J. I., Conn, G. L., Lane, A. N., and Brown, T. (1996) *Biochemistry 35*, 12538−12548.
14. Stein, C. A., Subasinghe, C., Shinozuka, K., and Cohen, J. S. (1988) *Nucleic Acids Res. 16*, 3209−3221.
15. Cummins, L., Graff, D., Beaton, G., Marshall, W. S., and Caruthers, M. H. (1996) *Biochemistry 35*, 8734−8741.
16. Damha, M. J., Wilds, C. J., Noronha, A., Brukner, I., Borkow, G., Arion, D., and Parniak, M. A. (1998) *J. Am. Chem. Soc. 120*, 12976−12977.
17. Rait, V. K., and Shaw, B. R. (1999) *Antisense Nucleic Acid Drug Dev. 9*, 53−60.
18. Vichier-Guerre, S., Pompon, A., Lefebvre, I., and Imbach, J.-L. (1994) *Antisense Res. Dev. 4*, 9−18.
19. Paoletti, J., Bazile, D., Morvan, F., Imbach, J.-L., and Paoletti, C. (1989) *Nucleic Acids Res. 17*, 2693−2704.
20. Lancelot, G., Guesnet, J.-L., and Vovelle, F. (1989) *Biochemistry 28*, 7871−7878.
21. Guesnet, J.-L., Vovelle, F., Thuong, N. T., and Lancelot, G. (1990) *Biochemistry 29*, 4982−4991.
22. Gmeiner, W. H., Rao, K. E., Rayner, B., Vasseur, J.-J., Morvan, F., Imbach, J.-L., and Lown, J. W. (1990) *Biochemistry 29*, 10329−10341.
23. Gmeiner, W. H., Rayner, B., Morvan, F., Imbach, J.-L., and Lown, J. W. (1992) *J. Biomol. NMR 2*, 275−288.
24. Bertrand, J.-R., Imbach, J.-L., Paoletti, C., and Malvy, C. (1989) *Biochem. Biophys. Res. Commun. 164*, 311−318.
25. Lavignon, M., Tounekti, N., Rayner, B., Imbach, J.-L., Keith, G., Paoletti, J., and Malvy, C. (1992) *Antisense Res. Dev. 2*, 315−324.
26. Debart, F., Tosquellas, G., Rayner, B., and Imbach, J.-L. (1994) *Bioorg. Med. Chem. Lett. 4*, 1041−1046.
27. Koga, M., Wilk, A., Moore, M. F., Scremin, C. L., Zhou, L., and Beaucage, S. L. (1995) *J. Org. Chem. 60*, 1520−1530.
28. Gagnor, C., Rayner, B., Leonetti, J.-P., Imbach, J.-L., and Lebleu, B. (1989) *Nucleic Acids Res. 17*, 5107−5114.
29. Boiziau, C., Debart, F., Rayner, B., Imbach, J.-L., and Toulmé, J.-J. (1995) *FEBS Lett. 361*, 41−45.
30. Aramini, J. M., van de Sande, J. H., and Germann, M. W. (1998) in *ACS Symposium Series 682: Molecular Modeling of Nucleic Acids* (Leontis, N. B., and SantaLucia, J., Jr., Eds.) pp 92−105, American Chemical Society, Washington, DC.
31. Tan, T. M. C., Kalisch, B. W., van de Sande, J. H., Ting, R. C. Y., and Tan, Y. H. (1998) *Antisense Nucleic Acid Drug Dev. 8*, 95−101.
32. Aramini, J. M., Kalisch, B. W., Pon, R. T., van de Sande, J. H., and Germann, M. W. (1996) *Biochemistry 35*, 9355−9365.
33. Aramini, J. M., van de Sande, J. H., and Germann, M. W. (1997) *Biochemistry 36*, 9715−9725.
34. Aramini, J. M., Mujeeb, A., and Germann, M. W. (1998) *Nucleic Acids Res. 26*, 5644−5654.
35. Aramini, J. M., and Germann, M. W. (1998) *Biochem. Cell. Biol. 76*, 403−410.
36. Brysch, W., Magal, E., Louis, J.-C., Kunst, M., Klinger, I., Schlingensiepen, R., and Schlingensiepen, K.-H. (1994) *Cancer Gene Ther. 1*, 99−105.
37. Vaughn, J. P., Iglehart, J. D., Demirdji, S., Davis, P., Babiss, L. E., Caruthers, M. H., and Marks, J. R. (1995) *Proc. Natl. Acad. Sci. U.S.A. 92*, 8338−8342.
38. Slamon, D. J., Clark, G. M., Wong, S. G., Levin, W. J., Ullrich, A., and McGuire, W. L. (1987) *Science 235*, 177−182.
39. Slamon, D. J., Godolphin, W., Jones, L. A., Holt, J. A., Wong, S. G., Keith, D. E., Levin, W. J., Stuart, S. G., Udove, J., Ullrich, A., and Press, M. F. (1989) *Science 244*, 707−712.
40. Fasman, G. D. (Ed.) (1975) *Handbook of Biochemistry and Molecular Biology. Nucleic Acids*, 3rd ed., Vol. I, p 589, CRC Press, Boca Raton, FL.
41. Breslauer, K. J. (1995) *Methods Enzymol 259*, 221−242.
42. Sklenár, V., Miyashiro, H., Zon, G., Miles, T., and Bax, A. (1986) *FEBS Lett. 208*, 94−98.
43. Sklenár, V., and Bax, A. (1987) *J. Magn. Reson. 74*, 469−479.
44. Piotto, M., Saudek, V., and Sklenár, V. (1992) *J. Biomol. NMR 2*, 661−665.
45. Lane, A. N. (1995) *Methods Enzymol. 261*, 413−435.
46. Borgias, B. A., and James, T. L. (1989) *Methods Enzymol. 176*, 169−183.
47. Borgias, B. A., and James, T. L. (1990) *J. Magn. Reson. 87*, 475−487.
48. Liu, H., Spielmann, H. P., Ulyanov, N. B., Wemmer, D. E., and James, T. L. (1995) *J. Biomol. NMR 6*, 390−402.
49. Liu, H., Thomas, P. D., and James, T. L. (1992) *J. Magn. Reson. 98*, 163−175.
50. Widmer, H., and Wüthrich, K. (1987) *J. Magn. Reson. 74*, 316−336.
51. Mujeeb, A., Kerwin, S. M., Kenyon, G. L., and James, T. L. (1993) *Biochemistry 32*, 13419−13431.
52. Saenger, W. (1984) *Principles of Nucleic Acid Structure*, Springer-Verlag, New York.
53. Wijmenga, S. S., Mooren, M. M. W., and Hilbers, C. W. (1993) in *NMR of Macromolecules; A Practical Approach* (Roberts, G. C. K., Ed.) pp 217−288, Oxford University Press, New York.
54. Pearlman, D. A., Case, D. A., Caldwell, J. W., Ross, W. S., Cheatham, T. E., III, Ferguson, D., M., Seibel, G. L., Singh, U. C., Weiner, P. K., and Kollman, P. A. (1995) *AMBER 4.1*, University of California, San Francisco, CA.
55. Schafmeister, C. E. A. F., Ross, W. S., and Romanovski, V. (1995) *LEaP (Version 1.0)*, University of California, San Francisco, CA.
56. Keepers, J. W., and James, T. L. (1984) *J. Magn. Reson. 57*, 404−426.
57. Borgias, B. A., and James, T. L. (1988) *J. Magn. Reson. 79*, 493−512.
58. Thomas, P. D., Basus, V. J., and James, T. L. (1991) *Proc. Natl. Acad. Sci. U.S.A. 88*, 1237−1241.
59. Lavery, R., and Sklenar, H. (1996) *Curves 5.1. Helical Analysis of Irregular Nucleic Acids*, Laboratoire de Biochimie Theorique, Centre National de la Recherche Scientifique, Paris, France.
60. Wüthrich, K. (1986) *NMR of Proteins and Nucleic Acids*, John Wiley & Sons, New York.
61. van Wijk, J., Huckriede, B. D., Ippel, J. H., and Altona, C. (1992) *Methods Enzymol. 211*, 286−306.
62. Schmitz, U., and James, T. L. (1995) *Methods Enzymol. 261*, 3−44.
63. van Wijk, J., Haasnoot, K., de Leeuw, F., Huckriede, D., and Altona, C. (1995) *PSEUROT 6.2. A Program for the Conformational Analysis of Five Membered Rings*, University of Leiden, Leiden, The Netherlands.
64. Pikkemaat, J. A., and Altona, C. (1996) *Magn. Reson. Chem. 34*, S33−S39.
65. Bhattacharyya, D., and Bansal, M. (1992) *J. Biomol. Struct. Dyn. 10*, 213−226.
66. González, C., Stec, W., Kobylanska, A., Hogrefe, R. I., Reynolds, M., and James, T. L. (1994) *Biochemistry 33*, 11062−11072.
67. Cheatham, T. E., III, and Kollman, P. A. (1997) *J. Am. Chem. Soc. 119*, 4805−4825.

68. Oda, Y., Iwai, S., Ohtsuka, E., Ishikawa, M., Ikehara, M., and Nakamura, H. (1993) *Nucleic Acids Res. 21*, 4690−4695.
69. Nishizaki, T., Iwai, S., Ohtsuka, E., and Nakamura, H. (1997) *Biochemistry 36*, 2577−2585.
70. Szyperski, T., Götte, M., Billeter, M., Perola, E., Cellai, L., Heumann, H., and Wüthrich, K. (1999) *J. Biomol. NMR 13*, 343−355.
71. Uchiyama, Y., Miura, Y., Inoue, H., Ohtsuka, E., Ueno, Y., Ikehara, M., and Iwai, S. (1994) *J. Mol. Biol. 243*, 782−791.
72. Crooke, S. T., Lemonidis, K. M., Neilson, L., Griffey, R., Lesnik, E. A., and Monia, B. P. (1995) *Biochem. J. 312*, 599−608.

BI9915418